Title
Mitigation of hydrogen crossover in liquid alkaline water electrolysers using gas recombination catalysts

Journal
Nature Energy

ISSN
2058-7546

Authors
Liu, Haotian
Lang, Jack T
Babbe, Finn
et al.

Publication Date
2026-06-26

DOI
10.1038/s41560-026-02094-7

nature energy

Article

https://doi.org/10.1038/s41560-026-02094-7

Mitigation of hydrogen crossover in liquid alkaline water electrolysers using gas recombination catalysts

Received: 5 August 2025

Accepted: 1 June 2026

Published online: 26 June 2026

Check for updates

Haotian Liu[1], Jack T. Lang[2], Finn Babbe[3], Dylan Bauer[1], Andres Marquez Rossy[4], Tomas Grejtak[4], Yuxiao He[5], Yu Huang[5,6,7], David A. Cullen[4], Iryna V. Zenyuk[2] & Xiong Peng[1]

The rising demand for hydrogen calls for improvements in the efficiency of liquid alkaline water electrolysers (LAWEs), which can be fulfilled by advanced electrodes or separators. Nevertheless, they also intensify hydrogen crossover and safety concerns, thus mandating efficient mitigation strategies. Here we studied the correlation between cathodes and hydrogen crossover behaviours and mitigated safety risks by designing a gas recombination catalyst (GRC). We attribute the elevated hydrogen crossover associated with platinum-based cathodes to their preferential utilization for the hydrogen evolution reaction that creates elevated hydrogen supersaturation, as evidenced by direct measurements of dissolved hydrogen concentration. Varying the placement of platinum layers relative to the cathode–separator interface also supports this conclusion. The implementation of a GRC reduces hydrogen crossover by 95% without affecting LAWE performance and functions for over 1,000 h at 1 A cm^{-2}. This study provides insights into hydrogen supersaturation and the crossover mechanism, as well as offering a promising pathway to enhance the efficiency and reliability of alkaline water electrolysis.

Liquid alkaline water electrolysers (LAWEs) have been a cornerstone of industrial hydrogen production and offer benefits through their low cost, longevity and technological maturity[1]. Research has projected an increasing global demand for hydrogen[2], highlighting the need to further advance the efficiency and reliability of LAWEs. LAWEs rely on porous separators for ion movement to sustain operation, which also introduces Ohmic resistance. One approach to improving LAWE efficiency is to minimize this Ohmic resistance, for example, by adopting a zero-gap design[3] or reducing the thickness of separators. One of the most widely used separators is the Zirfon diaphragm with a typical thickness of ~220 or 500 μm and a porosity of up to 75% (ref. 4), due to which hydrogen crossover can cause safety concerns through the formation of flammable gas mixtures[5].

Hydrogen supersaturation can drive molecular hydrogen crossover. Despite there being no direct evidence, hydrogen supersaturation is often invoked to explain the current-dependent hydrogen crossover and elevated fluxes that cannot be accounted for solely by hydrogen solubility[6–8]. This is plausible because when the dissolved hydrogen evolution rate exceeds the formation rate of gas bubbles, the local hydrogen concentration can pass the solubility limit and reach

[1]Energy Technologies and Systems Division, Lawrence Berkeley National Laboratory, Berkeley, CA, USA. [2]Department of Chemical and Biomolecular Engineering, University of California Irvine, Irvine, CA, USA. [3]Chemical Science Division, Lawrence Berkeley National Laboratory, Berkeley, CA, USA. [4]Materials Science and Technology Division, Oak Ridge National Laboratory, Oak Ridge, TN, USA. [5]Department of Materials Science and Engineering, University of California Los Angeles, Los Angeles, CA, USA. [6]Department of Chemistry and Biochemistry, University of California Los Angeles, Los Angeles, CA, USA. [7]California NanoSystems Institute, University of California Los Angeles, Los Angeles, CA, USA. e-mail: xiongp@lbl.gov

https://doi.org/10.1038/s41560-026-02094-7

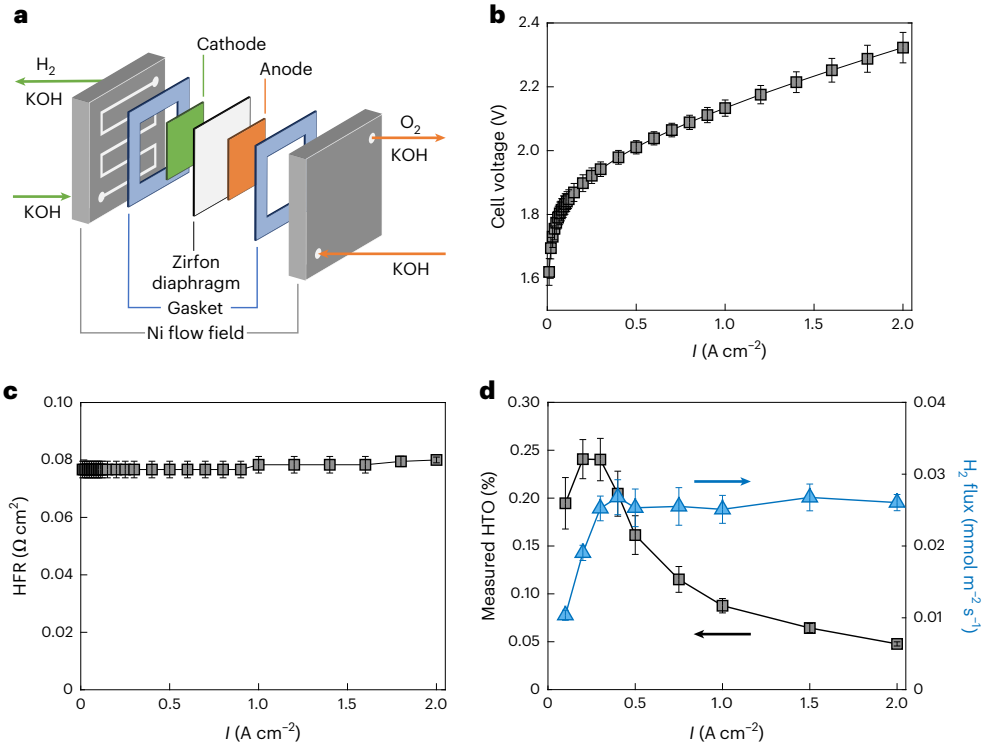

Fig. 1 | LAWE performance and hydrogen crossover using Ni electrodes. **a**, Schematic illustration of a typical three-layer electrode assembly in zero-gap LAWEs. **b**–**d**, Polarization curve (**b**), HFR profile (**c**), and measured HTO and hydrogen crossover flux from cathode to anode (**d**) in LAWEs using Ni foam as both the anode and cathode. Separator: Zirfon UTP 220; electrolyte: 7 M KOH; temperature: 80 °C. In **b**–**d**, the data are presented as averages and the error bars represent the standard deviation from at least three independent tests.

supersaturation. Electrolyte mixing has also been reported to cause high gas crossover[5]. However, under industrial settings, mature engineering degassing solutions are implemented before mixing[9]. Thus, the role of electrolyte mixing under degassing conditions in LAWEs remains unclear and merits further study.

When hydrogen reaches the low flammable limit (LFL), LAWEs can be subjected to unplanned shutdown, causing reverse current and degradation[10]. Although hydrogen crossover does not scale linearly with decreasing Zirfon thickness[11], further thinning (for example, 50–100 µm) would presumably exacerbate hydrogen crossover. Thus, minimizing Ohmic resistance by adopting thinner Zirfon diaphragms faces safety challenges. Such a trade-off has been previously simulated[12]. To reduce crossover, studies show that a delicate compensation of a liquid pressure differential or the introduction of finite gaps can be effective, although with a compromise to efficiency[13,14]. In our view, developing an effective hydrogen gas crossover mitigation strategy to achieve safety and efficiency improvements by adopting thinner separators than those currently used could be transformative.

Gas recombination catalysts (GRCs) have historically been prepared to mitigate hydrogen crossover by catalysing hydrogen consumption via the recombination reaction of $2H_2 + O_2 \rightarrow 2H_2O$ in proton exchange membrane water electrolysers (PEMWEs). For example, a spray-coated platinum (Pt) GRC was shown to achieve lower hydrogen crossover in PEMWEs[15]. In addition, a duo-recombination layer generated by reactive spraying was shown to enhance the durability of GRCs[16]. However, to our knowledge, GRCs have not been developed for use in LAWEs. Most GRC designs in PEMWEs rely on binders (for example, Nafion) for integrity and insulation from the anode, raising concerns that binders with low anionic conductivity may affect LAWE efficiency.

Moreover, more active electrodes than the widely used nickel (Ni) are desired to meet advanced performance metrics (for instance, US Department of Energy 2026 target: 1.0 A cm^{-2} at 1.8 V per cell)[17–19]. Although Ni electrodes have comparable oxygen evolution reaction (OER) activities to Pt-group metal (PGM) catalysts (for example, iridium or ruthenium oxides)[20,21], their hydrogen evolution reaction (HER) activities remain inferior to those of PGM-based counterparts (for example, Pt-based materials)[22–24]. As electricity prices drive water electrolysis costs[25], the levelized cost of produced hydrogen can be reduced using a Pt cathode with appropriate loading. As hydrogen is likely to be produced in a confined space within a thin catalyst layer when using Pt-based cathodes at low loadings, the resultant hydrogen supersaturation induced by cathode utilization may affect hydrogen crossover behaviour in LAWEs. However, such a correlation is yet to be investigated.

In this work, we observed a drastic difference in hydrogen crossover attributed to elevated hydrogen supersaturation with Pt cathodes compared with Ni cathodes, with direct evidence of hydrogen supersaturation supported by both in situ and in cell measurements. Varying the placement of Pt layers in LAWEs revealed that cathode utilization closely affects H_2 crossover and supersaturation. To mitigate H_2 crossover, a Pt-based GRC was designed that consumes over 95% of crossover hydrogen at 1 A cm^{-2} and remains stable for over 1,000 h.

Quantifying H_2 crossover in LAWEs

Using a laboratory set-up (Fig. 1a), LAWEs with Ni electrodes showed consistent performance (Fig. 1b) and high-frequency resistance (HFR; Fig. 1c), comparable to those previously reported[10]. H_2 crossover was quantified under electrolyte non-mixing and mixing conditions (Supplementary Figs. 1 and 2, respectively). Under electrolyte mixing, measurements were conducted with and without electrolyte degassing before mixing. Hydrogen-to-oxygen (HTO) values represent the percentage of hydrogen in the anode exhaust. Without degassing, higher HTOs were observed than under non-mixing conditions

https://doi.org/10.1038/s41560-026-02094-7

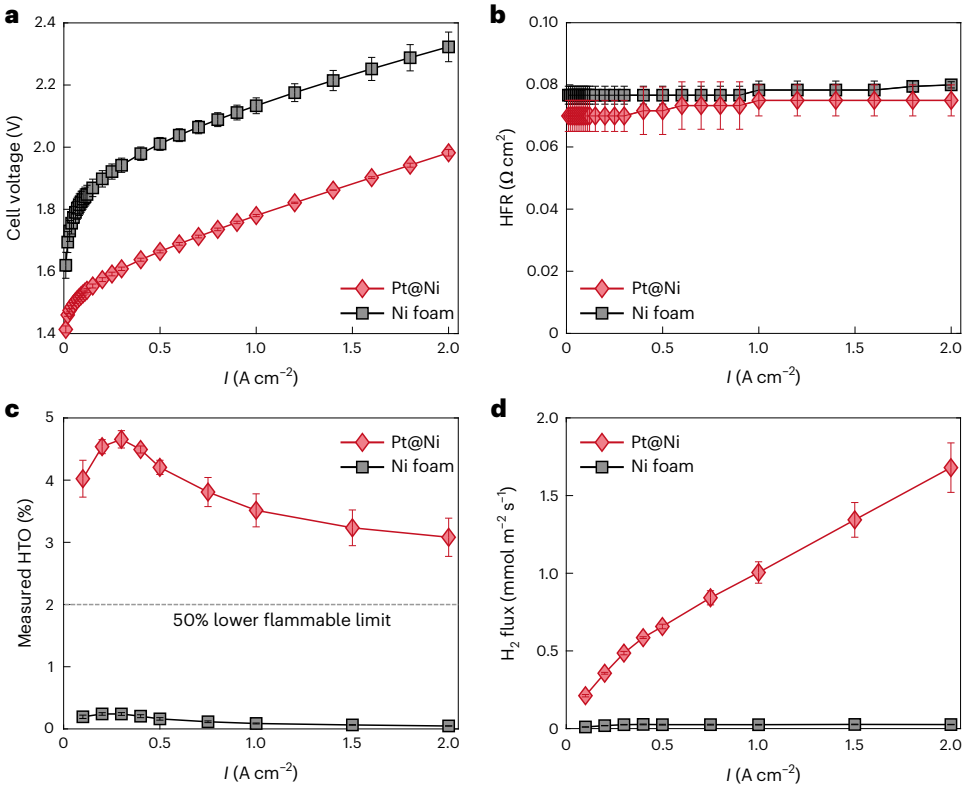

Fig. 2 | Comparison of LAWE performance and hydrogen crossover for Pt and Ni cathodes. a–**d**, Polarization curves (**a**), HFR profiles (**b**), measured HTO profiles (**c**) and hydrogen crossover flux (**d**) for Pt@Ni and Ni cathodes. Anode: Ni foam; cathode: Pt@Ni foam or Ni foam; separator: Zirfon UTP 220; electrolyte: 7 M KOH; temperature: 80 °C. The results are presented as averages and the error bars represent the standard deviation from at least three independent tests.

(Supplementary Fig. 3a), consistent with previous studies[5]. However, with degassing, identical HTO values were observed under mixing and non-mixing conditions (Supplementary Fig. 3b). These results indicate that degassing effectively suppresses the hydrogen crossover associated with electrolyte mixing, whereas crossover arising from intrinsic transport processes inside LAWEs cannot be mitigated by such engineering controls. Because electrolyte mixing without degassing produces mixing-dependent HTO values (Supplementary Note 1), the remainder of this study focused on hydrogen crossover under non-mixing conditions.

Compared with the typical trend of HTO monotonically decreasing with current, we observed that HTO initially increased in low currents (<0.3 A cm^{-2}) and then decreased as the current further increased (Fig. 1d). Experimental artefacts, including gas leakage, line connection, electrode size and gas residence time, were studied and their potential impacts on measurements were ruled out (Supplementary Notes 2–4). Because the observed discrepancy corresponds to a lower measured hydrogen crossover, meaning that a certain amount of hydrogen is consumed at the anode before being measured by gas chromatography (GC), we investigated possible mechanisms for this behaviour. The results show that the electrochemical oxidation of hydrogen at the Ni anode is negligible (Supplementary Note 5), whereas the chemical reaction between hydrogen and oxygen at the anode can consume hydrogen and account for the deviation in HTO trends (Supplementary Note 6). To our knowledge, such consumption has not been reported in LAWEs and requires future rigorous quantification. Nevertheless, an apparent kinetic model was employed to estimate and account for the chemical consumption of hydrogen, with the corrected HTO showing a monotonic decrease with current (Supplementary Note 6).

Given that the formation of flammable gas mixtures is a primary safety concern, measured HTO is used throughout this report for practical relevance unless specified otherwise, whereas hydrogen flux is reported as a combination of chemically consumed hydrogen determined by the model and gaseous hydrogen quantified by GC. Hydrogen flux exhibited a clear dependence on current density, with an initial increase from 0.1 to 0.3 A cm^{-2} (Fig. 1d). This continuous increase is attributed to an increasing supersaturation-induced concentration gradient at the cathode due to hydrogen diffusion. At higher current densities, the hydrogen flux plateaued as the enhanced oxygen evolution at the anode diluted the hydrogen content, resulting in a much lower HTO. To demonstrate the oxygen dilution effect, we assumed an ideal case in which hydrogen concentration at the cathode is at the solubility limit, leading to a nearly constant hydrogen flux (Supplementary Fig. 10a). As oxygen production increased with current, the hydrogen content dropped accordingly (Supplementary Fig. 10b), consistent with the oxygen dilution effect previously reported[7,26].

To pursue better efficiency, a Pt-coated Ni foam cathode was prepared through an electrodeposition process (denoted Pt@Ni). X-ray fluorescence (XRF) revealed that the deposited Pt exhibits a flower-like morphology and is evenly distributed across the Ni foam (Supplementary Fig. 11) at a Pt loading of 0.23 ± 0.04 mg cm^{-2} (Supplementary Table 1). The Pt@Ni cathode outperformed the Ni foam cathode (Fig. 2a), achieving a reduction in cell voltage of 340.8 ± 48.8 mV at 2 A cm^{-2}. This improvement is primarily due to a reduction of the cathode overpotential, as shown by three-electrode measurements (Supplementary Fig. 12). The Pt@Ni cathode also showed slightly lower HFRs than the Ni foam (Fig. 2b), likely due to the lower electronic resistance of electroplated Pt compared with Ni foam with possible oxide layers. The HTO of the Pt@Ni cathode was higher than that of the Ni cathode, with the highest HTO reaching 4.66 ± 0.14% (Fig. 2c). The LFL of hydrogen is generally accepted to be 4% (ref. 27), with a proposed lower threshold of 2% for industrial water electrolysis (International

https://doi.org/10.1038/s41560-026-02094-7

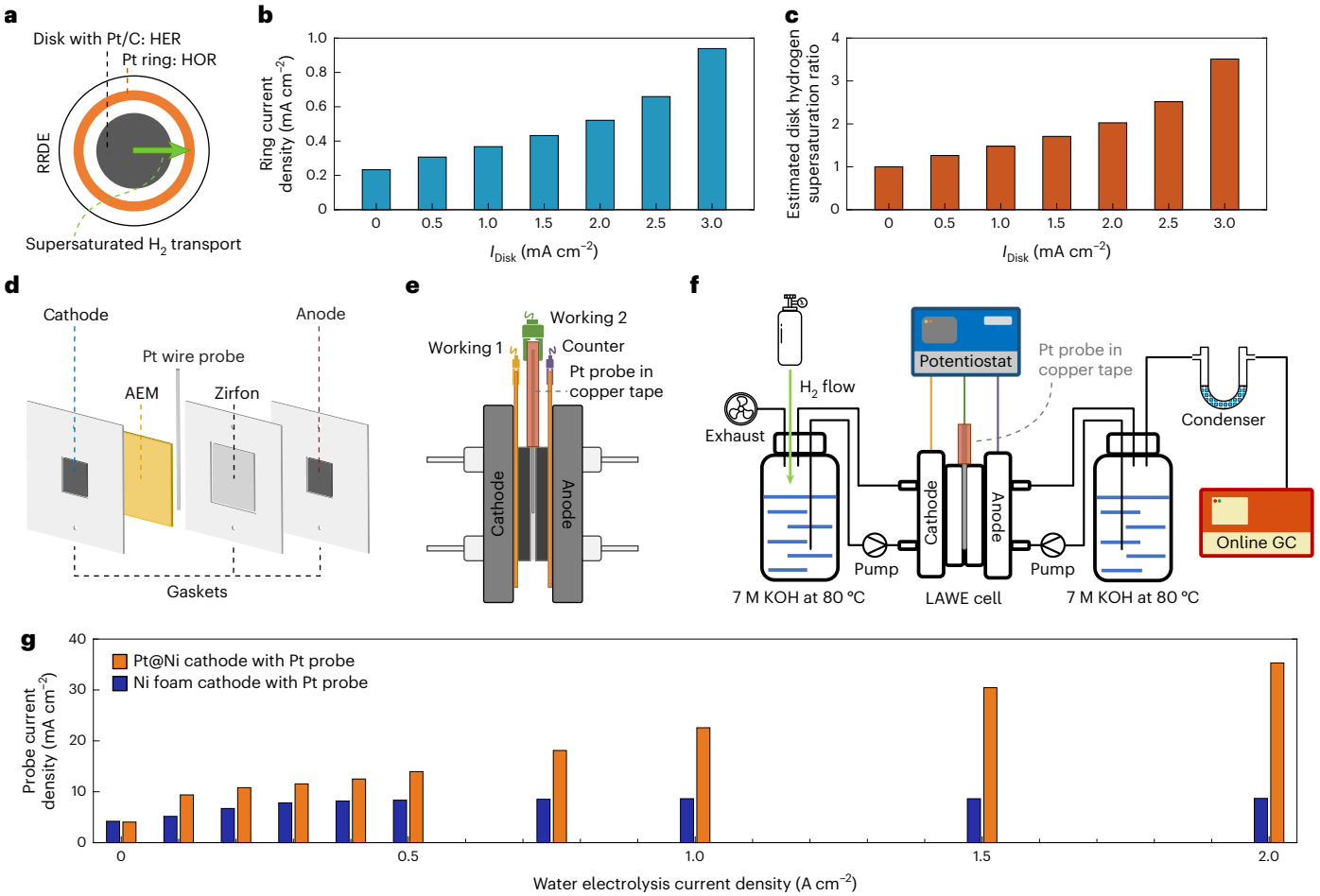

Fig. 3 | Direct probing of hydrogen supersaturation near the cathode during HER. a, Schematic top-view illustration of the RRDE set-up. Dissolved hydrogen generated at the disk electrode flows outwards and is oxidized by the Pt ring electrode. **b**, Collected ring current densities at different disk current densities. **c**, Estimated hydrogen supersaturation ratio at the disk electrode based on ring current. **d**–**f**, Schematic illustrations of the electrode assembly showing the position of the Pt wire probe (**d**), the cell-level set-up showing the cathode (working 1), the Pt wire probe (working 2) and the anode (counter) (**e**), and the system-level set-up (**f**) during measurements. The Pt wire exposed outside the cell is guided by a copper tape current collector. **g**, Current densities measured by the Pt wire probe at different applied water electrolysis current densities using Pt@Ni and Ni cathodes in LAWEs.

Organization for Standardization 22734)[28,29]. Thus, LAWEs with a Pt@Ni cathode can potentially exceed the LFL at certain current densities.

At a higher Pt loading (0.57 mg cm^{-2}, defined as Pt@Ni-H), the absolute electrochemical active surface area (ECSA) was quantified to be 1,025.0 cm^2, compared with 437.5 cm^2 for Pt@Ni (Supplementary Fig. 13). The specific ECSA of Pt@Ni-H and Pt@Ni was calculated to be 36.0 and 38.0 m^2 per g Pt, respectively, indicating that the enhancement of the absolute ECSA comes from Pt loading. Despite not showing an improved performance (Supplementary Fig. 13c,d), Pt@Ni-H achieved a lower hydrogen flux than Pt@Ni (Supplementary Fig. 13e). This is likely due to a lower specific current density as a result of its higher ECSA. At the same specific current density, we observed an identical hydrogen flux for Pt@Ni-H and Pt@Ni (Supplementary Fig. 13f). These results highlight how the Pt cathode can affect hydrogen crossover, which will be further discussed later. Nevertheless, compared with a Ni cathode, Pt@Ni showed a much higher hydrogen crossover (Fig. 2d). This is likely due to a higher hydrogen concentration gradient caused by a higher level of supersaturation. To probe this effect, hydrogen diffusivity through Zirfon was first quantified (Supplementary Note 7 and Supplementary Figs. 14 and 15).

Evidence and quantification of supersaturation

Before quantifying supersaturation, we used a rotating-ring disk electrode (RRDE) set-up (Fig. 3a) to experimentally validate its existence under HER conditions. The Pt ring electrode was set at 0.55 V versus the reversible hydrogen electrode (RHE) while various HER currents were applied to the Pt disk electrode. The Pt ring electrode can oxidize dissolved hydrogen in the electrolyte phase and produce a hydrogen oxidation reaction (HOR) current under mass-transport-limited conditions (Supplementary Fig. 16). Thus, as the HER current increases, when hydrogen supersaturation occurs, the HOR current is expected to increase. This hypothesis was verified experimentally (Fig. 3b). In addition, a HOR current remained measurable in the absence of an applied HER current (Fig. 3b) due to continuous hydrogen bubbling to ensure bulk electrolyte hydrogen saturation. The hydrogen concentration and supersaturation can be estimated using the Levich equation[30]. As the HER current increased, an increase in hydrogen supersaturation was observed (Fig. 3c). In these experiments, the disk current was limited to 3 mA cm^{-2}; above this, hydrogen bubbles covered the ring electrode, resulting in measurement variability. Nevertheless, these RRDE tests support the existence of hydrogen supersaturation under HER conditions.

To ensure translation of the observed hydrogen supersaturation from the RRDE to the LAWE, a Pt wire probe was applied between the Zirfon separator and cathode to measure the HOR current near the cathode (Fig. 3d–f). An anion exchange membrane (AEM) was placed between the Pt probe and cathode to avoid direct contact and interference from hydrogen bubbles (Fig. 3d). As cathode potentials

https://doi.org/10.1038/s41560-026-02094-7

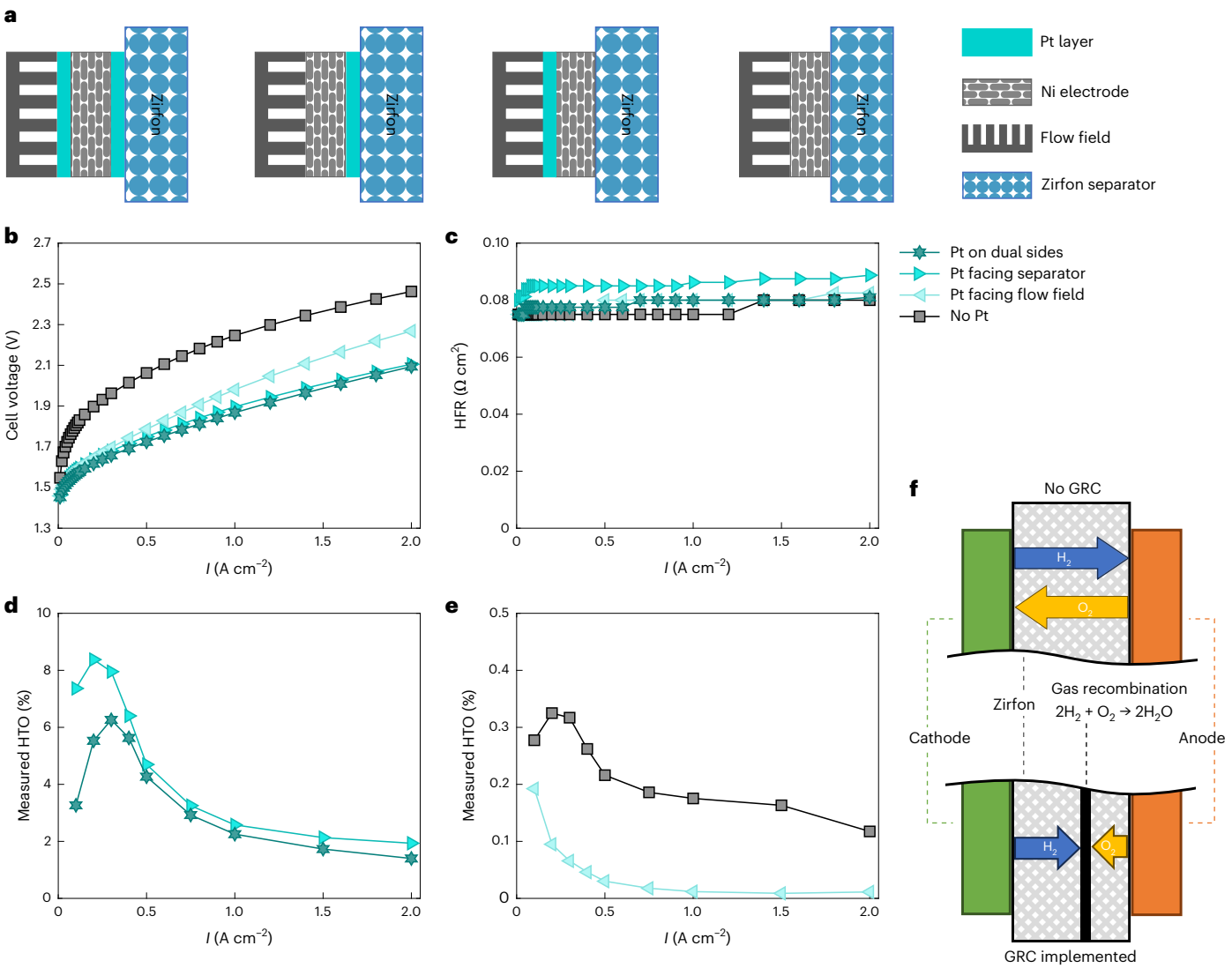

Fig. 4 | Pt location effect on LAWE performance and hydrogen crossover behaviour. a, Schematic illustrations of Pt layers at various locations in the cathode of LAWEs. From left to right, Pt layer at both the Zirfon–cathode and cathode–flow-field interfaces, Pt layer at the Zirfon–cathode interface, Pt layer at the cathode–flow-field interface and no Pt layer. **b**,**c**, Polarization curves (**b**) and HFR profiles (**c**) for various cathodes with a Pt layer facing the Zirfon separator and/or flow field. Data for a Ni cathode without Pt layers are also shown. **d**,**e**, Comparison of the HTO for LAWEs with various cathodes: with a Pt layer on both sides of the cathode and facing the Zirfon separator (**d**) and a Pt layer facing the flow field and a Ni cathode with no Pt layer (**e**). **f**, Schematic illustration of a GRC layer in LAWEs to mitigate H_2 crossover. Anode: Ni felt; cathode: Ni felt with Pt layer at different locations; separator: Zirfon UTP 220; electrolyte: 7 M KOH; temperature: 80 °C.

(versus RHE) were measured (Supplementary Fig. 12), the voltage applied between the Pt probe and cathode was adjusted to maintain a constant 0.6 V versus RHE to achieve a mass-transport-limited HOR current (Supplementary Fig. 17). A HOR current was measured in the absence of a water electrolysis current (Fig. 3g) due to hydrogen bubbling to ensure hydrogen saturation in the bulk catholyte. A higher HOR current was observed on applying an electrolysis current (Fig. 3g), indicating that the hydrogen concentration in the electrolyte passes the solubility limit and reaches supersaturation. Comparison of the HOR currents achieved for Ni and Pt@Ni cathodes shows that the latter creates a higher level of hydrogen supersaturation (Supplementary Fig. 18). However, the AEM introduced extra diffusional resistance and reduced hydrogen crossover compared with in regular LAWEs (Supplementary Fig. 19). Nevertheless, the RRDE and Pt probe measurements collectively provide direct evidence of hydrogen supersaturation during HER, supporting its quantification in LAWEs.

By using effective diffusivity to estimate hydrogen concentration ($c_{H_2}^{Ca}$; Supplementary Note 7), the supersaturation ratio (defined as the ratio between $c_{H_2}^{Ca}$ and the hydrogen concentration at the solubility limit[31]) can be calculated (Supplementary Fig. 20). The results show that $c_{H_2}^{Ca}$ is one to three orders of magnitude higher than the hydrogen solubility. This has also been observed in PEMWEs at a similar level of supersaturation[32–34]. As H_2 supersaturation occurs only with HER, the ratio is expected to reach close to unity at infinitesimal currents. Indeed, this is shown by linear regression of the H_2 supersaturation curves for both cathodes (Supplementary Fig. 20c,d).

The Pt@Ni cathode showed higher supersaturation than the Ni cathode (Supplementary Fig. 12a,b), leading to higher H_2 crossover (Fig. 2c). As H_2 supersaturation primarily occurs in regions where HER takes place, the root cause of the higher supersaturation for Pt@Ni than for Ni is attributed to discrepancies in cathode utilization. Ni active sites located at the Zirfon–cathode interface cannot sustain the operating current due to the limited HER activity and surface area,

https://doi.org/10.1038/s41560-026-02094-7

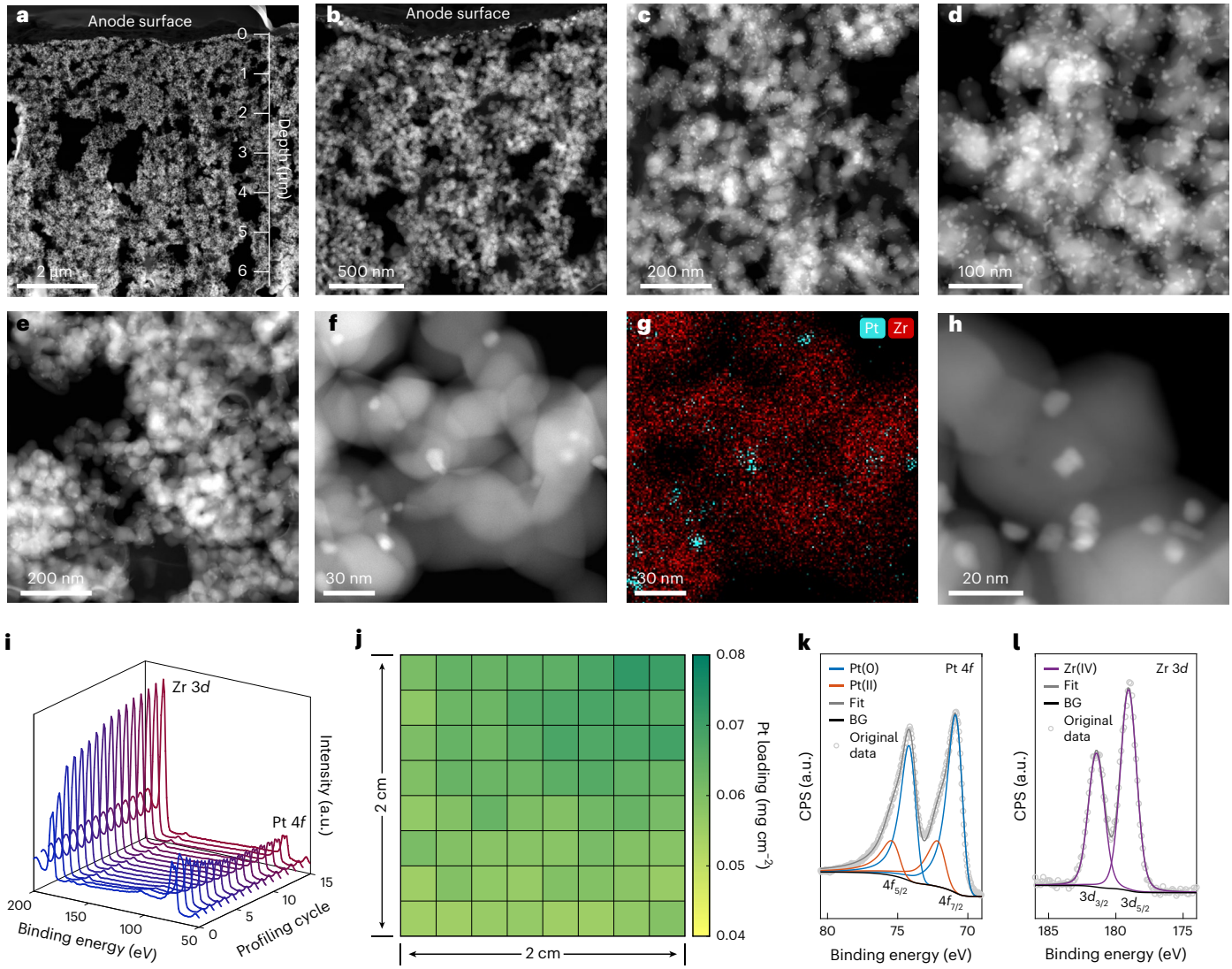

Fig. 5 | Design and characterization of Pt-GRC$_{An}$-Zirfon. a,**b**, Cross-sectional HAADF-STEM images of Pt-GRC$_{An}$-Zirfon near the anode surface. **c**,**d**, Slice view of Pt-GRC$_{An}$-Zirfon near the anode surface under HAADF-STEM, showing the distribution of Pt nanoparticles. **e**, Slice view of Pt-GRC$_{An}$-Zirfon under HAADF-STEM at a distance of 8 µm from the anode surface. **f**,**g**, HAADF-STEM image (**f**) and EDS mapping (**g**) showing sparsely dispersed Pt nanoparticles supported by ZrO_2 particles. **h**, HAADF-STEM image of Pt-GRC$_{An}$-Zirfon showing Pt nanoparticles supported by ZrO_2 and their size. **i**, XPS with depth profiling cycles. Profiling cycle = 0 represents the position at the anode surface; profiling cycles > 0 represent positions away from the anode surface. **j**, XRF mapping of 2 cm × 2 cm Pt-GRC$_{An}$-Zirfon, showing Pt in-plane loading distributions. **k**,**l**, XPS spectra of Pt 4*f* (**k**) and Zr 3*d* (**l**). CPS, counts per second; BG, background.

due to which utilization of the Ni cathode for HER is extended towards the flow field side. Therefore, less severe hydrogen supersaturation at the Zirfon–cathode interface can be expected. In contrast, owing to the high HER activity and creation of a high-surface-area Pt layer by electroplating[35], Pt@Ni cathode utilization is primarily located at the Zirfon–cathode interface. As a result, drastically higher hydrogen supersaturation is expected to occur at the Zirfon–cathode interface due to discrepancies in electrode utilization, which results in a much higher HTO and H_2 flux.

How cathode utilization affects LAWE performance and H_2 crossover

To verify this hypothesis, we fabricated cathodes by sputtering a Pt layer either on one side or both sides of the Ni substrate and placed them either at the Zirfon–cathode interface and/or cathode–flow-field interfaces (Fig. 4a). As sputtering is a line-of-sight coating method[36], Pt was only deposited on the surface rather than across the entire Ni structure, in contrast to electroplating. The sputtered Pt showed a smooth and uniform coverage of the Ni surface, with a thickness of ~400 nm (Supplementary Fig. 21). In addition, to further ensure a strict surface coating by Pt sputtering, Ni felt was chosen over Ni foam due to its denser surface and lower porosity, as evidenced by X-ray computed tomography (X-ray CT; Supplementary Figs. 22 and 23).

LAWEs with sputtered Pt layers on the cathode outperformed the Ni cathode, even when the Pt layer was located at the cathode–flow-field interface (Fig. 4b). This supports our hypothesis that Ni sites at the Zirfon–cathode interface are not sufficient to sustain operation and Ni cathode utilization for HER needs to be extended towards the flow field side. Otherwise, a similar performance of the Ni cathode and the cathode with a Pt layer at the cathode–flow-field interface should be expected. Identical performances were observed for LAWEs with a single Pt layer at the Zirfon–cathode interface and Pt layers at both the Zirfon–cathode and cathode–flow-field interfaces (Fig. 4b). This suggests that a Pt layer at the Zirfon–cathode interface is primarily responsible for supporting HER. The benefit of having a Pt layer near the Zirfon–cathode interface is to minimize OH^- ionic

https://doi.org/10.1038/s41560-026-02094-7

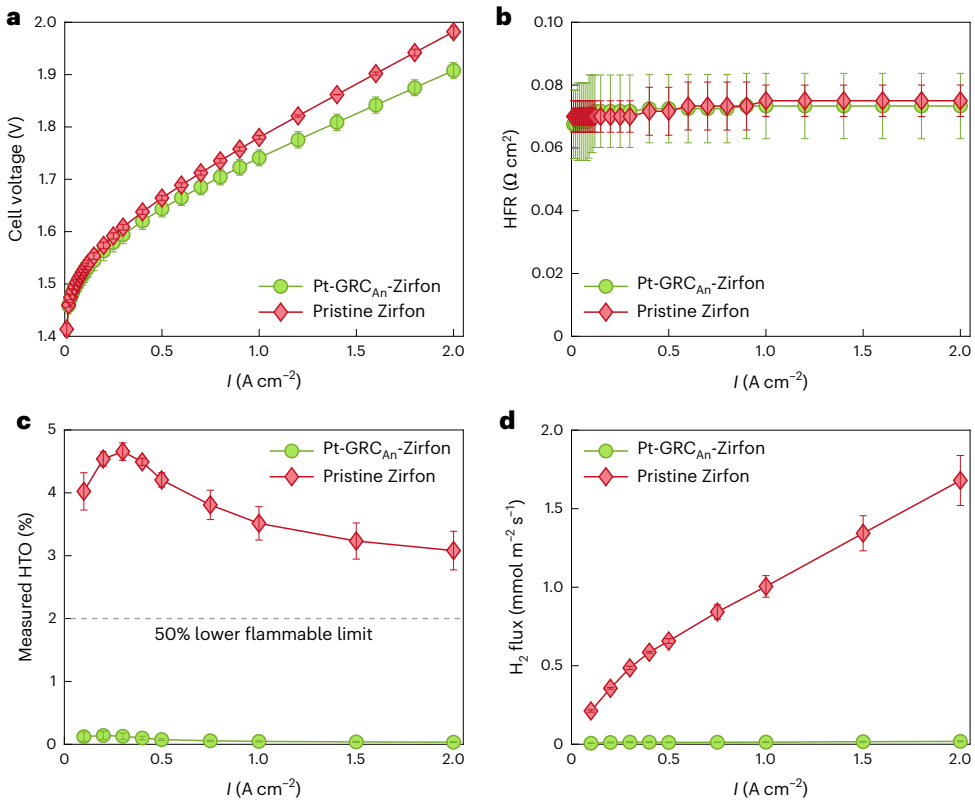

Fig. 6 | LAWE performance and hydrogen crossover profile with a GRC. a–d, Polarization curves (**a**), HFR profiles (**b**), measured HTO profiles (**c**) and hydrogen crossover flux profiles (**d**) for LAWEs with Pt-GRC_{An}-Zirfon and Zirfon UTP 220. Anode: Ni foam; cathode: Pt@Ni; separator: Pt-GRC_{An}-Zirfon or Zirfon UTP 220; electrolyte: 7 M KOH; temperature: 80 °C. The results are presented as averages and error bars represent the standard deviation from three independent tests.

resistance through the cathode, as evidenced by the better LAWE performance observed with a single Pt layer at the Zirfon–cathode interface rather than at the cathode–flow-field interface (Fig. 4b), despite similar HFRs (Fig. 4c).

These results imply that the majority of the hydrogen will be produced within a confined Zirfon–cathode interfacial space, resulting in high H_2 supersaturation and crossover. Indeed, hydrogen crossover was drastically higher when the Pt layer was located at the Zirfon–cathode interface than at the cathode–flow-field interface (Fig. 4d,e). This was also shown by comparing LAWEs with a Pt layer on both sides of the cathode and a single Pt layer at the cathode–flow-field interface (Fig. 4d,e). Interestingly, LAWEs with a Pt layer on both sides showed a slightly lower HTO than those with a single Pt layer at the Zirfon–cathode interface (Fig. 4d), especially in the low current region (<0.5 A cm^{-2}), while at higher currents (≥0.5 A cm^{-2}), similar HTOs were observed. This indicates that when currents are small, the kinetic benefit of partly utilizing Pt beyond the Zirfon–cathode interface surpasses the OH^- ionic resistance penalty through the cathode, which is also supported by the identical performance particularly at low currents under these two conditions.

It should also be noted that LAWEs with a single Pt layer located at the cathode–flow-field interface have an even lower HTO than those with a Ni felt (Fig. 4e) and Ni foam cathode (Figs. 1d and 4e). This is likely due to the combination of a longer hydrogen diffusion distance and facile removal of generated hydrogen through flow-field channels. Given these benefits, placing a Pt layer close to but not directly at the Zirfon–cathode interface could be a promising strategy, although the ionic resistance penalty needs to be balanced. Meanwhile, a higher HTO was observed with Ni felt than with Ni foam (Supplementary Fig. 24), likely resulting from structural differences (Supplementary Figs. 22 and 23). Collectively, these results highlight the structural impact of the Pt cathode on LAWE performance and H_2 crossover due to its preferential utilization for HER and corroborate the crossover difference of the Pt and Ni cathodes.

Mitigating crossover via GRC

Although causing higher H_2 crossover, the contribution to efficiency by the Pt cathode should take precedence in practical LAWE design. Therefore, a hydrogen crossover mitigation strategy must be developed to minimize safety concerns. Inspired by GRCs in PEMWEs, Pt-based GRCs could be a potential choice for LAWEs. However, a few factors need to be considered (Fig. 4f): a Pt-based GRC should be located closer to the anode to avoid oxygen deficiency for the gas recombination reaction as oxygen has a lower diffusivity than hydrogen[37]. A Pt-based GRC cannot be deposited across the entire Zirfon structure due to cell shorting concerns. Lastly, the Pt loading on the GRC should be low to balance cost. When Pt nanoparticles mixed with Nafion binder as the GRC were coated on the anode side of the Zirfon surface (Supplementary Fig. 25a), performance loss was observed due to high Ohmic loss, likely induced by the low anionic conductivity of the binder (Supplementary Fig. 25b,c). Therefore, a GRC design strategy specifically tailored for LAWEs is needed.

Hence, we developed a Pt-functionalized Zirfon separator (denoted Pt-GRC_{An}-Zirfon). As shown by the high-angle annular dark-field scanning transmission electron microscopy (HAADF-STEM) cross-sectional view, Pt-GRC_{An}-Zirfon has a highly porous structure (Fig. 5a,b) with a high population of Pt nanoparticles located near the anode (Fig. 5c,d). The through-plane distribution of Pt nanoparticles extends up to 8 µm beneath the anode surface, beyond which the population of Pt nanoparticles starts to drop (Fig. 5e versus Fig. 5c,d). The Pt nanoparticles are supported by ZrO_2 particles and have an average diameter of ~5 nm (Fig. 5f–h). The majority of the Pt nanoparticles are

https://doi.org/10.1038/s41560-026-02094-7

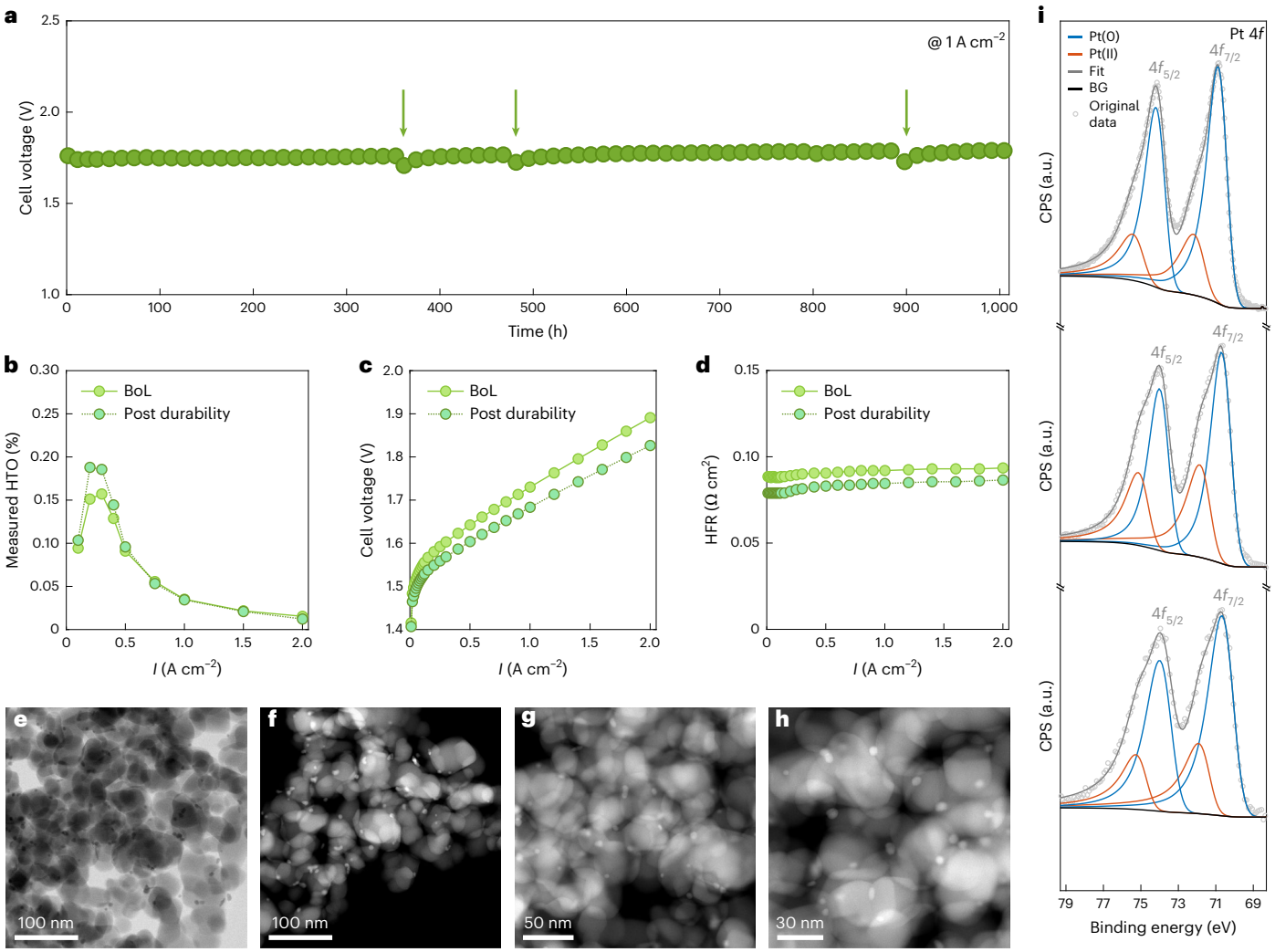

Fig. 7 | Durability of Pt-GRC$_{An}$-Zirfon in LAWEs. a, Chronopotentiometry curve recorded at 1 A cm^{-2}. The arrows denote interruptions and unplanned shutdowns during the durability test. **b**–**d**, Measured HTO profiles (**b**), polarization curves (**c**) and HFR profiles (**d**) of the BoL and post-durability cells. **e**–**h**, Microscopic images of post-durability Pt-GRC$_{An}$-Zirfon: high-resolution transmission electron microscopy (**e**) and HAADF-STEM (**f**–**h**) images showing sparsely distributed Pt particles. **i**, XPS spectra of pristine Zirfon UTP 220 (top), the post-durability Pt-GRC$_{An}$-Zirfon surface (middle) and post-durability Pt-GRC$_{An}$-Zirfon with the top surface removed (bottom). Anode: commercial Raney Ni mesh; cathode: commercial Pt–Ni mesh; separator: Pt-GRC$_{An}$-Zirfon; electrolyte: 7 M KOH; temperature: 80 °C.

isolated from each other, which is critical to minimize passivation by the anode potential. Furthermore, X-ray photoelectron spectroscopy (XPS) scans with depth profiling revealed a high Pt/Zr atomic ratio of 0.49:1 at the anode surface (Fig. 5i and Supplementary Fig. 26), with a drop in ratio as profiling proceeded (Supplementary Fig. 26 and Supplementary Table 2), whereas the cathode side displayed a ratio of less than 0.04 (Supplementary Table 3). These results confirm that the Pt nanoparticles are preferentially loaded on the anode side of Zirfon, which serves as the GRC at a preferred location.

XRF mapping revealed a uniform Pt in-plane distribution with a Pt loading of 0.062 ± 0.004 mg cm^{-2} (Fig. 5j). In addition, 69.5% of the Pt in Pt-GRC$_{An}$-Zirfon is in the metallic state (Fig. 5k), which is the active species for the gas recombination reaction rather than its oxide counterpart[38]. XPS also revealed that Zr remains in the valence state of IV (Fig. 5l), indicating that its low electronic conductivity is maintained. X-ray diffraction (XRD) revealed identical characteristic peaks of monoclinic ZrO_2 (JCPDS no. 37-1484) in pristine Zirfon and Pt-GRC$_{An}$-Zirfon (Supplementary Fig. 27). The Pt particles could not be detected by XRD and cross-sectional scanning electron microscopy (SEM; Supplementary Figs. 27 and 28) due to the low loading and small particle size. X-ray CT showed that the polysulfone matrix and ZrO_2 structures in pristine Zirfon were preserved in Pt-GRC$_{An}$-Zirfon (Supplementary Figs. 29 versus 30).

Pt-GRC$_{An}$-Zirfon LAWE performance and recombination efficacy

LAWEs with Pt-GRC$_{An}$-Zirfon outperformed those using pristine Zirfon (Fig. 6a), with a voltage reduction of 74 ± 18 mV. This improvement is not due to a change in the Ohmic resistance of the separator, as shown by a similar HFR (Fig. 6b). Instead, it can be attributed to the higher OER activity of the Pt nanoparticles on the anode surface of Zirfon than Ni (ref. 39). This is supported by the lower activation loss in the *iR*-free polarization curve and lower charge-transfer resistance (Supplementary Figs. 31 and 32). The possibility of HOR induced by Pt on the anode surface can be excluded due to the formation of oxides, which can result in the complete loss of HOR activity[40,41]. Crucially, the HTO and hydrogen flux were suppressed by over an order of magnitude with Pt-GRC$_{An}$-Zirfon compared with pristine Zirfon (Fig. 6c,d). The HTO and hydrogen flux profiles with Pt-GRC$_{An}$-Zirfon are also plotted separately in Supplementary Fig. 33 for better visualization.

Identical shapes and positions of the capillary pressure saturation curves (Supplementary Fig. 34) indicate that the pore network and hydrophilicity of pristine Zirfon is retained in Pt-GRC$_{An}$-Zirfon, which also corresponds to similar HFRs in LAWEs (Fig. 6b). Thus, the possibility of a change in the H_2 effective diffusivity resulting from changes in the pore network and hydrophilicity can be ruled out, as also shown by the identical diffusivities measured for Pt-GRC$_{An}$-Zirfon and pristine Zirfon ($(1.72 \pm 0.16) \times 10^{-9}$ and $(1.71 \pm 0.11) \times 10^{-9}$ m^2 s^{-1}). Therefore, the observed reduction in hydrogen crossover can be attributed to the incorporation of Pt nanoparticles, which catalyse the recombination of crossover H_2 with O_2.

We calculated the GRC efficacy as the percentage of the reduced H_2 flux in comparison with the H_2 flux without the GRC. At each investigated current density, Pt-GRC$_{An}$-Zirfon provided a high recombination efficacy of over 95% (Supplementary Fig. 35). In addition, due to a lower hydrogen concentration at the anode when employing the GRC, a steeper hydrogen concentration gradient is created between the cathode and anode, which drives more diffusional hydrogen towards the anode. This result shows that the loss in hydrogen yield due to the GRC is less than 0.1% (Supplementary Fig. 36 and Supplementary Note 8). Nevertheless, the importance of employing the GRC is to alleviate safety concerns and ensure more reliable LAWE systems, thereby enabling further reductions in separator thickness to enhance LAWE efficiency.

Pt-GRC$_{An}$-Zirfon durability in LAWEs

The durability of Pt-GRC$_{An}$-Zirfon was evaluated by holding a LAWE cell at 1 A cm^{-2} for 1,000 h. The cell performance remained stable for the testing period after an initial improvement (Fig. 7a), primarily due to the activation of Raney Ni (ref. 42). After the durability test, Pt-GRC$_{An}$-Zirfon still provided a high recombination efficacy, as evidenced by an almost unchanged HTO profile compared with that at the beginning of life (BoL; Fig. 7b). The polarization curve after the durability test revealed an even better performance than the BoL (Fig. 7c), in agreement with the observed initial improvement. Similar HFR values were observed before and after the durability tests (Fig. 7d), indicating the retention of ionic conductivity. The identical Pt loading (Supplementary Table 4), ZrO_2-supported morphology and distribution (Fig. 7e–h) also highlight the structural durability of Pt-GRC$_{An}$-Zirfon.

Even though Pt at the Zirfon surface can be oxidized under OER conditions, as indicated by the drop in metallic Pt from 67.6% to 56.2% (Fig. 7i), Pt particles at GRC locations can still remain in the metallic state. This is evidenced by the higher percentage of metallic Pt (63.2%) indicated by XPS. In addition, a separate durability test was conducted at 1 A cm^{-2} for 200 h. The metallic Pt fractions were measured to be 67.6%, 53.2% and 63.3% for BoL Pt-GRC$_{An}$-Zirfon, post-durability Pt particles on the anode surface and at GRC locations, respectively (Supplementary Fig. 37). The similar changes in the fraction of metallic Pt observed after 200 and 1,000 h indicate that Pt oxidation does not scale linearly with operation time, but instead predominantly occurs during the initial stages. These results highlight the critical role of sparsely dispersed Pt particles on the ZrO_2 surface in limiting interparticle connections (Fig. 5a–h), thereby avoiding fast oxidation at the anode.

The durability was further studied under dynamic operation conditions to mimic operation/shutdown in LAWEs (Supplementary Fig. 38a). During the 2,000-cycle test, the cell voltage initially dropped and then plateaued (Supplementary Fig. 38b), consistent with the 1,000-h durability test (Fig. 7a). From a zoom-in view of the first ten cycles (Supplementary Fig. 38c), the cell slowly discharged under open-circuit voltage conditions, which is consistent with a previous study[43]. Comparison of the polarization curves and HFR and HTO profiles of the BoL and post-cycled cells further confirmed the operational durability of Pt-GRC$_{An}$-Zirfon and indicated its versatility for dynamic operation (Supplementary Fig. 38d–f).

Conclusions

A Pt@Ni cathode can drastically boost LAWE performance while also causing higher hydrogen crossover compared with Ni cathodes. This is attributed to elevated hydrogen supersaturation caused by preferential utilization of Pt active sites for HER. In situ RRDE and in cell measurements to quantify the localized hydrogen concentration near the cathode confirmed that the hydrogen concentration exceeds its solubility limit, thereby proving the presence of hydrogen supersaturation. A GRC effectively mitigates this hydrogen crossover, consuming more than 95% of the hydrogen crossing over, and exhibits outstanding durability at 1 A cm^{-2} for over 1,000 h. The results of our study imply that further reducing the thickness of the Zirfon separator could boost efficiency while ensuring safe operation in LAWEs. Similar catalyst design principles can be extended to many emerging electrochemical devices for the mitigation of gas crossover.

Methods

Chemicals and materials

MSE PRO porous nickel foam was purchased from MSE Supplies. Ni felt was purchased from Bekaert (18-025). Pt mesh (99.9% trace metals basis), Pt black (powder, ≤20 µm, ≥99.95% trace metals basis), KOH (ACS reagent, ≥85%, pellets), sodium borohydride ($NaBH_4$, powder, ≥98.0%), boric acid (H_3BO_3, ACS reagent, ≥99.5%), sodium citrate tribasic dihydrate (ACS reagent, ≥99.0%) and chloroplatinic acid ($H_2PtCl_6{\cdot}6H_2O$, ACS reagent, ≥37.50% Pt basis) were purchased from Sigma-Aldrich. All reagents were used as received without further purification. Zirfon UTP 220 was purchased from Agfa-Gevaert. Kapton tape was purchased from McMaster-Carr. The electrodes used for durability tests were provided by Verdagy[44]. Piperion AEMs (20 µm) were purchased from Fuel Cell Store. Cell fixtures, including stainless steel endplates, brass current collectors and Ni flow fields, were purchased from Fuel Cell Technologies. The RRDE was purchased from Pine Research Instrumentation. Deionized water (18 MΩ cm^{-1}) was obtained from an ultrapure purification system (Milli-Q advantage A10).

Pt electrodeposition on Ni foam (Pt@Ni)

Typically, a piece of Ni foam (3 cm × 4 cm) was cut and clipped onto an electrode clip as the working electrode. The electrolyte solution comprised 0.8 mM $H_2PtCl_6{\cdot}6H_2O$, 0.75 M H_3BO_3 and 0.05 M sodium citrate in water. Pt mesh was used as the counter electrode. A potential of −3 V was applied for 10 min. After reaction, the electrodeposited Pt@Ni foam was washed with water ready for use.

Pt sputtering on Ni felt

Typically, a piece of Ni felt (7 cm × 7 cm) was secured on the sputtering plate with Kapton tape. The sputtering machine was operated at a power of 150 W under Ar atmosphere for ~41 min to achieve a Pt layer thickness of 400 nm. The Pt-sputtered Ni felt was then ready for use.

Fabrication of Pt-GRC$_{An}$-Zirfon

The Pt-based GRC was grown on Zirfon using a facile infiltration–reduction method. Typically, Kapton tape was washed with water to reduce its stickiness, preventing damage when peeling off the Zirfon. Then, the treated Kapton tape was placed and secured on one side of the Zirfon. The masked Zirfon was placed in a flask containing 80 ml of 0.08 mg ml^{-1} $H_2PtCl_6{\cdot}6H_2O$ solution and stirred for 12 h. After infiltration, the Zirfon was placed in a flask of water to wash out excess of the Pt salt. Then, the Zirfon was placed in another flask containing 80 ml of 2 mg ml^{-1} $NaBH_4$ solution for 12 h to reduce the Pt ions. After the reaction, the exposed side of Zirfon turned black and the masking Kapton tape was carefully removed. The Pt-GRC$_{An}$-Zirfon was stored in water before LAWE testing.

LAWE cell electrode assembly

A standard Fuel Cell Technology cell with two 5-cm^2 serpentine flow fields was used for LAWE cell testing. Electrodes were cut into a 5-cm^2 square shape using a laser. When Ni foam with a thickness of 0.3175 mm was used for the electrodes, 0.3048-mm-thick polytetrafluoroethylene (PTFE) gaskets were used to control the compression level. The same gaskets were used for the Pt@Ni foam, which had the same thickness as the Ni foam. For Ni felt with a thickness of 0.2921 mm, 0.2794-mm-thick PTFE gaskets were used. Zirfon UTP 220 with a thickness of 0.2286 mm was used as the separator and a 0.2286-mm-thick PTFE gasket was used to match the thickness. The cell was clamped with a pair of brass current collectors and a pair of stainless steel endplates using eight bolts. Each bolt was wrenched to a torque of 4.52 Nm in increments of 1.13 Nm. The cell configuration used to measure the effective diffusivity and hydrogen crossover activation energy was similar, but no electrode was installed and no current was applied.

LAWE performance tests and crossover measurement

A 7 M KOH solution at 80 °C was fed into the cell at a flow rate of 20 ml min^{-1} and the cell was kept at this temperature with a cell heater during measurement. Before acquiring the polarization curves, a cyclic voltammetry test from 1.0 to 2.2 V (for the Ni cathode) or 1.0 to 1.8 V (for the Pt–Ni cathode) was conducted for cell conditioning. The polarization curves were then collected using chronopotentiometry, with each current held for 20 s. The average potential of the last 5 s was used to determine the polarization curves. Galvanostatic electrochemical impedance spectroscopy (GEIS) was used to determine the Ohmic resistance of the cell. Measurements were taken over a frequency range of 1 Hz to 100 kHz, with the signal amplitude set to 5% of the applied current or 200 mA (whichever was less). HFRs were determined by GEIS fitting using an equivalent circuit including a series combination of a resistor and two of resistor connected in parallel with constant-phase element (RCPE).

Crossover was measured using the same LAWE cell design. In addition, the gas outlet from the anode electrolyte bottle was connected to a condenser to trap water vapour in the anodic gas exhaust. The ensuing dried gas product then flowed into a gas chromatograph equipped with a thermal conductivity detector (TCD) and a sampling loop of 100 µl to measure the hydrogen content. A gas flow meter was connected to the GC outlet to monitor the rate of gas flow. The hydrogen content was calculated from the hydrogen peak area from the TCD, which was calibrated using standard gas mixtures with known hydrogen content.

LAWE three-electrode performance tests

The three-electrode LAWE cell assembly featured a potential-sensing AEM incorporated inside. Typically, a Versogen AEM was cut into a strip 8 cm long and 0.8 cm wide. The strip was inserted between the cathode and separator gaskets, touching the Zirfon but not the cathode. The strip extending outside the cell fixture was immersed in a home-made reference tube containing 7 M KOH. A Hg/HgO reference electrode was placed in the same reference tube for potential sensing. Before acquiring polarization curves, a cyclic voltammetry test from 0 to 0.8 V (versus Hg/HgO) was performed on the working electrode for cell conditioning. The polarization curves were collected using chronopotentiometry, with each current held for 20 s. The average potential of the last 5 s was used to determine the polarization curves. GEIS was used to determine the Ohmic resistance of the cell. Measurements were taken over a frequency range of 1 Hz to 100 kHz, with the signal amplitude set to 5% of the applied current or 200 mA (whichever was less). HFRs were determined by GEIS fitting using an equivalent circuit including a series combination of a resistor and two RCPEs.

ECSA measurement of Pt@Ni and Pt@Ni-H

ECSAs were measured in 1 M KOH with Pt@Ni or Pt@Ni-H as the working electrode, a Pt mesh with a similar geometric area was used as the counter electrode and Hg/HgO was used as the reference electrode. The electrolyte was saturated with nitrogen before tests. A cyclic voltammetry scan from 0.05 to 1.10 V versus RHE was conducted at a scan rate of 0.02 V s^{-1}. ECSAs were determined by integrating the hydrogen underpotential deposition region of the cyclic voltammogram after double-layer correction, assuming a charge density of 210 µC cm^{-2} for a monolayer of hydrogen on polycrystalline Pt.

Effective diffusivity and hydrogen crossover activation energy measurements

The set-up for the effective diffusivity and hydrogen crossover activation energy measurements was similar to the set-up used for crossover measurement. A 7 M KOH solution was flowed through the cathode chamber at 20 ml min^{-1} and hydrogen was continuously bubbled into the catholyte at 25 ml min^{-1} to ensure a stable hydrogen concentration at the solubility limit. A 7 M KOH solution was flowed through the anode chamber at 20 ml min^{-1} and argon was continuously bubbled into the anolyte at 14 ml min^{-1} (the exact flow rate was monitored by a flow meter). The gas outlet from the anode electrolyte bottle was connected to a condenser to trap moisture in the exhaust gas, which then flowed into an online gas chromatograph equipped with a TCD to quantify the hydrogen that diffused to the anode. A flow meter was installed at the outlet of the GC to measure the flow rate.

Measurement and hydrogen supersaturation estimation at the RRDE

An RRDE with a fixed glassy carbon disk loaded with 0.04 mg Pt per cm^2 and a Pt ring was used as the working electrode. The disk diameter was 4.57 mm and the inner and outer diameters of the ring were 4.93 and 5.88 mm, respectively. The disk and the ring were separated by a 0.18-mm-thick PTFE layer. The working electrode was rotated at a rate of 1,600 r.p.m. The nominal collection efficiency of the ring was 22%. The electrolyte consisted of a 0.1 M KOH solution saturated with hydrogen. Pt wire was used as the counter electrode and Hg/HgO as the reference electrode. A current density of 0–3 mA cm^{-2} with a step of 0.5 mA cm^{-2} was applied to the disk, while a potential of 0.55 V versus RHE was applied to the ring to oxidize hydrogen.

Note that gaseous hydrogen could not be oxidized by the ring due to the lack of ionic conductivity. The rising HOR current at the ring was due only to the dissolved/supersaturated hydrogen supplied by the disk. Thus, the ring current collected in the absence of an applied disk current (i_0) was used as the baseline. The Levich current (i_L) can be theoretically calculated by the Levich equation (1):

$$i_L = 0.620\, nFAD^{\frac{2}{3}}\omega^{\frac{1}{2}}\nu^{-\frac{1}{6}}c_{H_2,\mathrm{disk}} \quad (1)$$

where n is the charge-transfer number, F is Faraday's constant, A is the disk area, D is the hydrogen diffusion coefficient, ω is the rotating rate, ν is the kinematic viscosity of the electrolyte and $c_{H_2,\mathrm{disk}}$ is the hydrogen concentration generated by the disk HER. For these measurements, n, F, A, D, ω and ν were constant. Equation (1) can be simplified as equation (2):

$$i_L = k\, c_{H_2,\mathrm{disk}} \quad (2)$$

where k is defined by equation (3):

$$k = 0.620\, nFAD^{\frac{2}{3}}\omega^{\frac{1}{2}}\nu^{-\frac{1}{6}} \quad (3)$$

When HER occurs at the disk, the extra current collected at the ring ($i_{\mathrm{ring,add}}$) from HOR can be calculated using equation (4):

$$i_{\mathrm{ring,add}} = i_{\mathrm{ring}} - i^0_{\mathrm{ring}} \quad (4)$$

where i_{ring} is the ring current and i^0_{ring} is the ring current in the absence of an applied disk current. Considering that the ring has a collection

efficiency (N) of only 22%, $i_{ring,add}$ can also be calculated using equation (5):

$$i_{ring,add} = N i_L \quad (5)$$

By definition, the hydrogen supersaturation ratio at the disk ($S_{H_2,disk}$) can be calculated using equation (6):

$$S_{H_2,disk} = \frac{c_{H_2,disk}}{c^0_{H_2}} + 1 \quad (6)$$

where $c^0_{H_2}$ is the hydrogen solubility. After combining equations (2)–(4), $S_{H_2.disk}$ can be calculated using equation (7):

$$S_{H_2,disk} = \frac{i_{ring} - i^0_{ring}}{N k c^0_{H_2}} + 1 \quad (7)$$

Thus, the hydrogen supersaturation ratio at the disk under different applied HER currents can be calculated. (The H_2 diffusion coefficient in 0.1 M KOH, H_2 solubility in 0.1 M KOH and kinematic viscosity of 0.1 M KOH can be obtained from the literature[37,45–47].)

This estimated supersaturation ratio is the minimum theoretical number from our calculation. In practice, the HER–HOR reaction pair is not only limited by Levich mass transfer, but is also generally a mixed-control process described by the Koutecký–Levich equation. Moreover, the collection efficiency of 22% is the highest theoretically achievable, without accounting for liquid-phase hydrogen loss due to bubbling across the disk–ring gap. All these factors will reduce the current that can be collected at the ring. Therefore, our calculation will underestimate the supersaturation ratio, yielding the minimum value.

Measurement of HOR current using a Pt probe in LAWE

The configuration of the LAWE electrode assembly with a sandwiched Pt probe was similar to a regular LAWE assembly, but a Pt wire (0.050-mm diameter) was placed between the cathode and Zirfon as a separate working electrode. A 20-µm Piperion AEM was also placed between the Pt probe and cathode to prevent electrical contact between the probe and electrolysis cathode. Pt wire that was exposed outside the cell was secured using copper tape. A 7 M KOH solution at 80 °C was fed into the cell at a flow rate of 20 ml min^{-1} and the cell was kept at this temperature with a cell heater during measurement. The catholyte was saturated with hydrogen during testing. The potentiostat was set to the mode for two working electrodes sharing a common counter electrode. Before starting water electrolysis, chronoamperometry was conducted by applying 0.6 V (versus RHE) to the Pt probe to acquire the baseline HOR current. Then we started water electrolysis at designated fixed current densities, while the Pt probe was kept at 0.6 V versus RHE to record HOR currents. Each chronoamperometry session lasted ~30 s until stable. Hydrogen crossover profiles of the cell with an AEM and Pt probe were accessed using the same set-up.

Hydrogen crossover flux and GRC efficiency calculation

The hydrogen crossover flux (J_{H_2}) was calculated on the basis of the measured HTO and oxygen flow rate (V_{O_2}). Assuming that the Faradaic efficiency of OER is 100%, the theoretical oxygen flow generated can be calculated using equation (8):

$$V_{O_2} = \frac{I \times V_m}{4F} \quad (8)$$

where I is the current and V_m is the molar volume of gas (~22.4 l mol^{-1} at standard temperature and pressure). As generating 1 mol of oxygen needs 4 mol of electrons, a coefficient of 4 is added. Thus, the hydrogen crossover flux can be calculated using equation (9):

$$J_{H_2} = \frac{V_{O_2} \times x^{GC}_{H_2}}{A} \quad (9)$$

where A is the electrode active area and $x^{GC}_{H_2}$ is the hydrogen content measured by GC.

The GRC efficacy (E_{GRC}) was calculated as the hydrogen flux reduction percentage before ($J_{H_2,noGRC}$) and after ($J_{H_2,GRC}$) applying the GRC, as shown in equation (10):

$$E_{GRC} = 1 - \frac{J_{H_2,noGRC}}{J_{H_2,GRC}} \quad (10)$$

Ultrasonic spray of Pt black on Zirfon UTP 220

Pt-black-loaded Zirfon UTP 220 was prepared by an ultrasonic spray method. Typically, the ink consisted of 16.3 mg Pt black, 7.05 g propanol and 3.26 g Nafion D521 solution (5 wt%). The solution was agitated with a sonication tip for 30 min in an ice bath to homogenize. A 6 cm × 6 cm piece of Zirfon UTP 220 was secured on the spraying bed by means of a vacuum and heated to 60 °C. Then the ink was sprayed using a SonoTek ultrasonic sprayer at a flow rate of 0.2 ml min^{-1} and nozzle power of 1.2 W at a frequency of 120 kHz. The spraying proceeded until the Pt loading reached ~0.06 mg cm^{-2}, as confirmed by XRF.

Gas breakthrough measurement

The set-up for capillary pressure measurement consisted of a customized stainless steel pressure cell. The sample was die-cut as a 19.05-mm-diameter circular disk. PTFE toroidal-shaped gaskets with a 19.05-mm inner diameter and 1-inch outer diameter were stacked around the sample to a total height of 220 µm. The sample was positioned between a hydrophilic polyvinylidene fluoride layer at the bottom and a hydrophobic PTFE layer on top. The hydrophilic layer was presoaked with water, ensuring that all bubbles were removed, and secured with suction. The mass of water moving in and out of the sample was recorded using an analytical balance to quantify the saturation of water imbibed into the sample. A correction for the evaporation of water on the analytical balance was implemented. The gas pressure inside the cell was controlled by a syringe pump and quantified with a pressure sensor. The gas pressure was increased or decreased at a continuous rate of ~0.2 kPa min^{-1}, controlled by the syringe pump.

Characterization

Surface morphologies and compositions were characterized by SEM and energy-dispersive X-ray spectroscopy (EDS; FEI Quanta FEG 250). Samples were placed in the chamber under high vacuum conditions (<2×10^{-5} torr) and the energy level of the beam was set to 10 kV. XRD patterns were collected using a Rigaku Smartlab X-ray diffractometer equipped with a HyPix-3000 high-energy-resolution two-dimensional multidimensional semiconductor detector. XRD measurements were performed by setting the same Rigaku SmartLab diffractometer to the Bragg–Brentano mode at room temperature. High-resolution transmission electron microscopy and HAADF-STEM measurements were conducted using a 200-kV FEI monochromated F20 UT Tecnai instrument. The surface compositions of the samples were investigated by XPS (Kratos Axis Ultra DLD) at take-off angles of 0 and 60° relative to the surface normal. Measurements were conducted at room temperature and under an ultrahigh vacuum of 7.5×10^{-9} torr. A monochromatic Al Kα source ($h\nu$ = 1,486.6 eV) was used to excite the core-level electrons of the materials. Spectral analysis was conducted using CasaXPS analysis software. XPS with depth profiling was carried out using the same set-up. Specifically, an Ar ion gun with a power of 1 kV and 600 nA was directed onto a raster area of 7.8 mm^{-2} on the investigated samples.

Each profile cycle took 5 min. Elemental ratios were calculated from the XPS spectra using integrated peak areas and relative sensitivity factors. XRF (Bruker) was used to quantify the Pt loading on all Pt-containing samples. Pt was sputtered using a radio frequency sputtering system (AJA, 99.999% Pt from Kurt Lasker). For cross-sectional analysis of Pt-GRC$_{An}$-Zirfon using STEM, small portions of the separator were embedded in epoxy and then cut by diamond-knife ultramicrotomy, targeting a specimen thickness of ~75 nm. HAADF-STEM and EDS images were recorded using a JEM-ARM200F NEOARM analytical electron microscope (JEOL) operated at 200 kV. Ex situ X-ray CT was performed at the Advanced Light Source at Lawrence Berkeley National Laboratory (Beamline 8.3.2) with a Pioneering in Cameras and Optoelectronics (PCO) Edge Charge-coupled Device (CCD) camera, a LuAg scintillator and ×20 optical lenses. The resulting images had a resolution of 0.323 µm voxel^{-1} and a horizontal field of view of 1.8 mm. Samples were prepared for tomography imaging by cutting the samples into 2 mm × 2 mm square sections, each having an ~45° tip and 5 mm base for mounting on the pins, which were mounted on the beamline rotating stage. A multilayer monochromator was used to select the X-ray energy of 20 keV. An exposure time of 300 ms was used.

Data availability

The data that support the findings of this study are available within the article and its Supplementary Information. Source data are provided with this paper.

References

1. Xia, Y., Cheng, H., He, H. & Wei, W. Efficiency and consistency enhancement for alkaline electrolyzers driven by renewable energy sources. *Commun. Eng.* **2**, 22 (2023).
2. *Global Hydrogen Review 2021* (IEA, 2021); https://www.iea.org/reports/global-hydrogen-review-2021
3. Wang, G. et al. Understanding performance limitation of liquid alkaline water electrolyzers. *J. Electrochem. Soc.* **171**, 064501 (2024).
4. Vermeiren, P., Adriansens, W., Moreels, J. P. & Leysen, R. Evaluation of the Zirfon® separator for use in alkaline water electrolysis and Ni-H_2 batteries. *Int. J. Hydrogen Energy* **23**, 321–324 (1998).
5. Trinke, P. et al. Hydrogen crossover in PEM and alkaline water electrolysis: mechanisms, direct comparison and mitigation strategies. *J. Electrochem. Soc.* **165**, F502 (2018).
6. Trinke, P., Bensmann, B. & Hanke-Rauschenbach, R. Current density effect on hydrogen permeation in PEM water electrolyzers. *Int. J. Hydrogen Energy* **42**, 14355–14366 (2017).
7. Gawas, R., Kushner, D. I., Peng, X. & Mukundan, R. Importance of hydrogen oxidation reaction current in quantifying hydrogen crossover in PEM water electrolyzers at high differential pressure. *Energy Environ. Sci.* https://doi.org/10.1039/D5EE00048C (2025).
8. Martinho, D. L. & Berning, T. A conceptual approach to reduce the product gas crossover in alkaline electrolyzers. *Membranes* **15**, 206 (2025).
9. Pere, G. Installation for degassing and recycling the electrolyte in an electrolyzer for producing gas. US patent US4379044A (1983).
10. Wang, G. et al. Probing electrode transformation under dynamic operation for alkaline water electrolysis. *Adv. Energy Mater.* **15**, 2500886 (2025).
11. Brauns, J. et al. Evaluation of diaphragms and membranes as separators for alkaline water electrolysis. *J. Electrochem. Soc.* **168**, 014510 (2021).
12. de Groot, M. T., Kraakman, J. & Garcia Barros, R. L. Optimal operating parameters for advanced alkaline water electrolysis. *Int. J. Hydrogen Energy* **47**, 34773–34783 (2022).
13. Wu, T., Zhou, Y., Yuan, F., Yang, Q. & Liu, B. Effects of trans-diaphragm liquid flow on hydrogen-in-oxygen in alkaline water electrolysis. *Int. J. Hydrogen Energy* **105**, 1393–1399 (2025).
14. Lira Garcia Barros, R., Kraakman, J. T., Sebregts, C., van der Schaaf, J. & de Groot, M. T. Impact of an electrode-diaphragm gap on diffusive hydrogen crossover in alkaline water electrolysis. *Int. J. Hydrogen Energy* **49**, 886–896 (2024).
15. Klose, C. et al. Membrane interlayer with Pt recombination particles for reduction of the anodic hydrogen content in PEM water electrolysis. *J. Electrochem. Soc.* **165**, F1271 (2018).
16. Zeng, Z. et al. Innovative duo-recombination layer design for effective hydrogen crossover mitigation in advanced MEAs for PEM water electrolyzers. *Int. J. Hydrogen Energy* **114**, 534–544 (2025).
17. Ehlers, J. C., Feidenhans'l, A. A., Therkildsen, K. T. & Larrazábal, G. O. Affordable green hydrogen from alkaline water electrolysis: key research needs from an industrial perspective. *ACS Energy Lett.* **8**, 1502–1509 (2023).
18. Sebbahi, S. et al. A comprehensive review of recent advances in alkaline water electrolysis for hydrogen production. *Int. J. Hydrogen Energy* **82**, 583–599 (2024).
19. Zhang, L. et al. Sodium-decorated amorphous/crystalline RuO_2 with rich oxygen vacancies: a robust pH-universal oxygen evolution electrocatalyst. *Angew. Chem. Int. Ed.* **60**, 18821–18829 (2021).
20. Sugawara, Y., Nakase, Y., Anilkumar, G. M., Kamata, K. & Yamaguchi, T. Oxygen evolution activity of nickel-based phosphates and effects of their electronic orbitals. *Nanoscale Adv.* **7**, 456–466 (2025).
21. Yan, H. et al. Anion-modulated HER and OER activities of 3D Ni–V-based interstitial compound heterojunctions for high-efficiency and stable overall water splitting. *Adv. Mater.* **31**, 1901174 (2019).
22. Ferriday, T. B., Middleton, P. H. & Kolhe, M. L. Review of the hydrogen evolution reaction—a basic approach. *Energies* **14**, 8535 (2021).
23. Zhao, Z. et al. Surface-engineered PtNi-O nanostructure with record-high performance for electrocatalytic hydrogen evolution reaction. *J. Am. Chem. Soc.* **140**, 9046–9050 (2018).
24. Wan, C. et al. Amorphous nickel hydroxide shell tailors local chemical environment on platinum surface for alkaline hydrogen evolution reaction. *Nat. Mater.* **22**, 1022–1029 (2023).
25. Mayyas, A. T., Ruth, M. F., Pivovar, B. S., Bender, G. & Wipke, K. B. *Manufacturing Cost Analysis for Proton Exchange Membrane Water Electrolyzers* Report No. NREL/TP-6A20-72740 (National Renewable Energy Laboratory, 2019).
26. Witte, J. et al. Influence of contact pressure on hydrogen crossover and polarization behavior in AEM water electrolysis. *J. Electrochem. Soc.* **172**, 014502 (2025).
27. Najjar, Y. S. H. Hydrogen safety: the road toward green technology. *Int. J. Hydrogen Energy* **38**, 10716–10728 (2013).
28. *ISO 22734:2019. Hydrogen Generators Using Water Electrolysis—Industrial, Commercial, and Residential Applications* (ISO, 2019).
29. Qi, R. et al. Pressure control strategy to extend the loading range of an alkaline electrolysis system. *Int. J. Hydrogen Energy* **46**, 35997–36011 (2021).
30. Levich, V. G. *Physicochemical Hydrodynamics* (Prentice-Hall, 1962).
31. Ilevbare, G. A., Liu, H., Edgar, K. J. & Taylor, L. S. Maintaining supersaturation in aqueous drug solutions: impact of different polymers on induction times. *Cryst. Growth Des.* **13**, 740–751 (2013).
32. Shibata, S. Supersolubility of hydyogen in acidic solution in the vicinity of hydrogen-evolving platinum cathodes in different surface states. *Denki Kagaku oyobi Kogyo Butsuri Kagaku* **44**, 709–712 (1976).
33. Chen, Q., Luo, L. & White, H. S. Electrochemical generation of a hydrogen bubble at a recessed platinum nanopore electrode. *Langmuir* **31**, 4573–4581 (2015).

34. Dukovic, J. & Tobias, C. W. The influence of attached bubbles on potential drop and current distribution at gas-evolving electrodes. *J. Electrochem. Soc.* **134**, 331 (1987).
35. Mahmood, N. et al. Electrocatalysts for hydrogen evolution in alkaline electrolytes: mechanisms, challenges, and prospective solutions. *Adv. Sci.* **5**, 1700464 (2018).
36. Lee, J. K. et al. Ionomer-free and recyclable porous-transport electrode for high-performing proton-exchange-membrane water electrolysis. *Nat. Commun.* **14**, 4592 (2023).
37. Tham, M. J., Walker, R. D. Jr & Gubbins, K. E. Diffusion of oxygen and hydrogen in aqueous potassium hydroxide solutions. *J. Phys. Chem.* **74**, 1747–1751 (1970).
38. Lalik, E. et al. Humidity induced deactivation of Al_2O_3 and SiO_2 supported Pd, Pt, Pd-Pt catalysts in H_2+O_2 recombination reaction: the catalytic, microcalorimetric and DFT studies. *Appl. Catal. A* **501**, 27–40 (2015).
39. Reier, T., Oezaslan, M. & Strasser, P. Electrocatalytic oxygen evolution reaction (OER) on Ru, Ir, and Pt catalysts: a comparative study of nanoparticles and bulk materials. *ACS Catal.* **2**, 1765–1772 (2012).
40. Sheng, W. et al. Correlating hydrogen oxidation and evolution activity on platinum at different pH with measured hydrogen binding energy. *Nat. Commun.* **6**, 5848 (2015).
41. Zalitis, C. M., Sharman, J., Wright, E. & Kucernak, A. R. Properties of the hydrogen oxidation reaction on Pt/C catalysts at optimised high mass transport conditions and its relevance to the anode reaction in PEFCs and cathode reactions in electrolysers. *Electrochim. Acta* **176**, 763–776 (2015).
42. Delgado, D., Bizzotto, F., Zana, A. & Arenz, M. Accelerated durability test for high-surface-area oxyhydroxide nickel supported on Raney nickel as catalyst for the alkaline oxygen evolution reaction. *ChemPhysChem* **20**, 3147–3153 (2019).
43. Gankhuyag, T., Obata, K. & Takanabe, K. Potential regulation for stable electrocatalysts in alkaline water electrolyzers during dynamic on and off operation through double-layer capacitance engineering. *J. Phys. Chem. C* **129**, 18043–18050 (2025).
44. Cole, K. M., Patterson, N., Zeng, J., Awara, M. & Albrecht, T. A. In-operando impedance spectroscopy study for accelerated lifetime studies of dynamic alkaline water electrolysis under industrial conditions. *Int. J. Hydrogen Energy* **137**, 125–130 (2025).
45. Ruetschi, P. & Amlie, R. F. Solubility of hydrogen in potassium hydroxide and sulfuric acid. Salting-out and hydration. *J. Phys. Chem.* **70**, 718–723 (1966).
46. Davis, R. E., Horvath, G. L. & Tobias, C. W. The solubility and diffusion coefficient of oxygen in potassium hydroxide solutions. *Electrochim. Acta* **12**, 287–297 (1967).
47. Hodges, A. et al. Critical analysis of published physical property data for aqueous potassium hydroxide. Collation into detailed models for alkaline electrolysis. *J. Chem. Eng. Data* **68**, 1485–1506 (2023).

Acknowledgements

We acknowledge the use of facilities at the Molecular Foundry supported by the Office of Science, Office of Basic Energy Sciences, of the U.S. Deparment of Energy under contract no. DE-AC02-05CH11231 and resources of the Advanced Light Source, a DOE Office of Science User Facility under contract no. DE-AC02-05CH11231. STEM research was conducted as part of a user project at the Center for Nanophase Materials Sciences (CNMS), which is a DOE Office of Science User Facility at Oak Ridge National Laboratory. We acknowledge Verdagy for supplying commercial electrode materials. We also acknowledge A. Kosakian, P. Rudnicki, R. Mukundan and A. Weber for thoughtful discussions and valuable suggestions. The views expressed in this article do not necessarily represent the views of the DOE or the US government.

Author contributions

H.L. performed the majority of the electrode/separator fabrication, characterization, cell testing and data analysis. D.B. also performed electrode fabrication and cell testing. J.T.L. performed X-ray CT measurements under the supervision of I.V.Z. F.B. performed the XPS and XRD measurement and analysis. A.M.R. performed the SEM-EDS analysis and T.G. performed the FIB and STEM analysis under the supervision of D.A.C. Y. He performed electron spectroscopy analysis under the supervision of Y. Huang. X.P. conceived the project. All authors contributed to the writing of the paper. H.L. and X.P. are the primary authors of the paper and chiefly responsible for all of the experimental design and data analysis.

Funding

We received funding from the Department of Energy, Office of Critical Mineral and Energy Innovation, the Fuel Cell Technologies programme (DOE-CMEI-HFTO) and the H2 from Next-generation Electrolyzers of Water (H2NEW) consortium (contract no. DE-AC02-05CH11231).

Competing interests

H.L. and X.P. have submitted an invention disclosure to the Intellectual Property Office at Lawrence Berkeley National Laboratory. The other authors declare no competing interests.

Additional information

Supplementary information The online version contains supplementary material available at https://doi.org/10.1038/s41560-026-02094-7.

Correspondence and requests for materials should be addressed to Xiong Peng.

Peer review information *Nature Energy* thanks Thomas Turek and the other, anonymous, reviewer(s) for their contribution to the peer review of this work. Peer reviewer reports are available.